Research Square

Preprints are preliminary reports that have not undergone peer review.
They should not be considered conclusive, used to inform clinical practice,
or referenced by the media as validated information.

Spectral Evidence for a Traveling Dynamo Wave in the Sunspot Butterfly Diagram

Martin Seilmayer

martin.seilmayer@dhsn.de

Duale Hochschule Sachsen

Research Article

Keywords: Sun Spot, Lomb Scargle, Spectral Analysis

Posted Date: July 30th, 2026

DOI: https://doi.org/10.21203/rs.3.rs-10242068/v1

License: This work is licensed under a Creative Commons Attribution 4.0 International License.
Read Full License

Additional Declarations: No competing interests reported.

Spectral Evidence for a Traveling Dynamo Wave in the Sunspot Butterfly Diagram

Martin Seilmayer[1*]

[1*]Staatliche Studienakademie Bautzen, Duale Hochschule Sachsen, Löbauer Straße 1, Bautzen, 02526, Saxony, Germany.

Corresponding author(s). E-mail(s): martin.seilmayer@gmail.com;

Abstract

Sunspot observations from 1825 to 2025 are analyzed as a two-dimensional dataset in time and latitude. The butterfly diagram emerges with each sunspot group assigned a binary information from magnetic polarity. Applying a multivariate Lomb–Scargle method, we compute the 2D power spectrum of this spatiotemporal distribution. The spectrum reveals that significant power is organized along ridges of constant phase velocity, which is the spectral signature of a modulated traveling wave. The dominant ridge corresponds to the observed equatorward migration of sunspot activity, with an average phase velocity derived from the butterfly wings. Next, the 22-year Hale cycle appears not as a single peak but as four distinct components (e. g. **21.6 yrs** and **26 yrs**), whose beating reproduces the canonical Hale period. Shorter periodicities (harmonics) and longer secular cycles (Gleissberg, Eddy, Hallstatt) align along same phase-velocity ridges, indicating they are physically coupled side bands of the underlying dynamo wave rather than independent oscillations. These findings support the interpretation of the sunspot butterfly diagram as the surface manifestation of a coherent, propagating dynamo wave, consistent with mean-field theory predictions.

Keywords: Sun Spot, Lomb Scargle, Spectral Analysis

1 Introduction

Since the beginning of the 17th century, systematic visual observations of Sunspots have provided a unique window into the dynamic processes occurring within the solar interior. These surface features are not merely isolated phenomena; their appearance

and migration patterns render fundamental features of the underlying solar dynamo. Historically, these patterns have been characterized by the 11 yrs Schwabe [1, 2] cycle for its appearance or the typically 22 yrs Hale cycle [3] for investigations on magnetic field distribution.

Since the 1820s, systematic observations of Sunspots have provided a two-dimensional dataset in time and latitude, commonly visualized as the butterfly diagram. This diagram exhibits an almost symmetric, wing-like structure that reflects the spatiotemporal organization of solar activity. While individual Sunspot groups represent localized magnetic features, the butterfly diagram captures their collective behavior as a macroscopic pattern as evidence of the solar cycle.

Early theoretical work by [4] established the foundation of solar dynamo theory, describing the interaction between magnetic fields and convective plasma flows in the solar interior. In this framework, magnetic fields are generated and amplified by differential rotation and turbulent convection, and subsequently transported radially outward. Due to convection and diffusion processes, magnetic flux emerges at the solar surface, where it becomes visible as Sunspots—regions of reduced temperature associated with concentrated magnetic fields.

The systematic equatorward migration of Sunspot activity is therefore interpreted as a consequence of the propagation of large-scale magnetic structures. In mean-field dynamo theory, this behavior is described by dynamo waves, whose direction and speed are governed by the interplay between differential rotation and the α-effect [5]. As a result, the butterfly diagram can be understood as the surface manifestation of magnetic patterns propagating through the solar interior.

Modern numerical simulations and theoretical models, e. g. [6, 7] support this interpretation and reproduce key features of the observed migration. At the same time, the equatorward drift has motivated alternative or complementary explanations based on flux-transport dynamos, in which meridional circulation plays a crucial role in advecting magnetic flux [8, 9]. Despite differences in detail, both approaches imply the existence of coherent, propagating wave–like structures underlying the observed Sunspot distribution. This perspective naturally raises the question whether the butterfly diagram can be quantitatively interpreted as a propagating wave in latitude–time space, a hypothesis that we investigate in the present work.

However, traditional one-dimensional analyses of Sunspot group data are inherently limited to resolve the complex interplay between the spatial (latitudinal) and temporal dimensions. Most established approaches rely on global solar indices, such as Wolf numbers R or general Sunspot numbers R_z, which, by definition, aggregate the rich latitudinal information of Sunspot occurrence data into a time series or probabilistic density function. Counting Sunspots per month or year acts as a form of numerical averaging and therefore emphasizes the dominant 22 yr Hale cycle while suppressing lower-amplitude variability or obscuring the relationship between neighboring frequencies. As a result, the spectrum of these indices is typically dominated by a single broad peak, making it difficult to disentangle overlapping processes or to identify coherent structures that evolve simultaneously in space and time.

While recent studies have highlighted significant periodicities in diverse solar indices, ranging from the 10.8 yr variation in solar radius [10, 11] to short-term oscillations in solar flare activity [12, 13], these signals are often treated as separate phenomena. Mathematical or numerical investigation often connect these frequencies to a solar dynamo model. Nevertheless, counting Sunspot events and the reduction to a 1D time series, in established analysis, obscures the fact that these disparate periods may actually be manifestations of the same underlying traveling wave.

In this paper, we propose that the Sunspot occurrence, depicted as butterfly diagram, is best understood as a complex and modulated traveling wave in more than one dimension. In general, the independent variables longitude, latitude and the date of occurrence could be taken into consideration. With respect to data availability, this work relies on longitude and time dependencies. To this end, we retain the latitudinal information of Sunspot occurrence and analyze the data in two dimensions using a multivariate Lomb–Scargle periodogram (LSM), which is well suited for evaluating the power spectral density of irregularly sampled datasets [14]. In contrast to one-dimensional methods, it preserves the coupling between latitude and time and allows for the identification of structures that are coherent across both dimensions.

A key diagnostic emerging from this analysis is the phase-velocity relation $v = (f_{\mathrm{Lat}} P_{\mathrm{Yrs}})^{-1}$,which links latitudinal and temporal scales. Here f_{Lat} depicts the latitudinal frequency and $P_{\mathrm{Yrs}} = f_{\mathrm{Yrs}}^{-1}$ corresponds the the period scale. An independently estimated drift velocity from the butterfly diagram defines a corresponding locus in spectral space.

We show that enhanced spectral power is preferentially concentrated in the vicinity of this phase-velocity relation, forming a broadened ridge rather than a sharply defined line, which is consistent with the spectral signature of a modulated traveling wave. In the context of this work, a ridge denotes a concentration of spectral power distributed along a line in $(f_{\mathrm{Lat}}, P_{\mathrm{Yrs}})$ space, rather than at isolated points. Hereafter, the line of constant phase velocity is named v-line.

Consequently, the two-dimensional analysis separates the individual wave components along a characteristic ridge, and suggests that they are coupled components of an underlying dynamo process.

Finally, the spectrum allows the data driven conclusion, that major cycles like Hale-cycle, Gleissberg, and Suess de Vries cycles, refer to [15, 16], are also connected to the same modulated traveling wave as short term periods originating from solar flare activity [12, 17] in a day scale or quasi biennial variations [18] on a two year scale or even variations of the solar radius on a decade scale. Next to that, we demonstrate that multivariate decomposition can separate overlapping signals from noise, such as those found in solar flare data or even a long term ≈ 2000 yrs Hallstatt cycle [16]. Of course the latter is highly speculative, but can be identified in the time series anyway.

In the following sections, we describe the data preparation and segmentation of the butterfly diagram, present the two-dimensional spectral analysis, and discuss the implications of the observed phase-velocity structure for the interpretation of solar activity.

2 Data Preparation

The foundation of this analysis is a consolidated dataset of Sunspot observations spanning two centuries (1825–2025), integrating records from the Royal Greenwich Observatory– USAF/NOAA(SOON)[1][19–21], as well as historical observations by Schwabe[2][22] and Spörer[3][25].

The complete data set originates "as-is" from [26] and is appended by recent records from NOAA [27]. A detailed discussion of the data collection is given by [26, 28] and the referenced literature. Unlike traditional solar indices such as the Wolf Number (R) or the International Sunspot Number (R_z), which aggregate Sunspot counts and sizes into a single monthly or yearly scalar, we treat each Sunspot group as a discrete sampling point in a 2D spatial-temporal plane.

Polarity assignment

To each Sunspot group n, we assign a binary polarity value $P_n \in \{-1, 1\}$ based on its hemisphere within the specific solar cycle and its mean latitude L_n at year Y_n. This approach interprets the Sunspot data as a series of impulse samples

$$P(Y, L) = \sum_n P_n \cdot \delta(Y - Y_n, L - L_n) \tag{1}$$

where $\delta(L, Y)$ is the two dimensional Dirac delta function. By utilizing a binary ± 1 assignment to each sample, we effectively eliminate the need of temporal averaging. Moreover, this ensures that the spectral analysis is sensitive to frequency and propagation velocity of the wave across all scales.

Hemispheric Segmentation and Slope Optimization

The butterfly diagram exhibits a distinct, wing-like symmetry across the solar equator, reflecting the equatorward migration of the modulated wave. To analyze these "wings" as coherent wave packets, we apply a segmentation procedure that assigns each Sunspot group to a specific solar cycle g.

The segmentation is achieved through the optimization of two piece-wise linear function that defines the boundaries between successive cycles in both the Northern and Southern hemispheres. The line of segmentation is defined as

$$l(Y) = \begin{cases} m_1 \, (Y - T_0) & m_1 < 0, L > 0 \\ m_2 \, (Y - T_0) & m_2 > 0, L \leq 0 \end{cases}, \tag{2}$$

which provides an intersection point $\{T_0, 0\}$. The dependent variables Y and L describe the time in years and latitude in degrees respectively. The individual slopes

[1] Available at http://solarscience.msfc.nasa.gov/greenwch.shtml and http://fenyi.solarobs.epss.hun-ren.hu/en/databases/DPD/

[2] Available at simbad.cds.unistra.fr/simbad/sim-basic?Ident=2015A%26A...584A..73S&submit=SIMBAD+search

[3] the reader might also refer to the historic publications [23, 24]

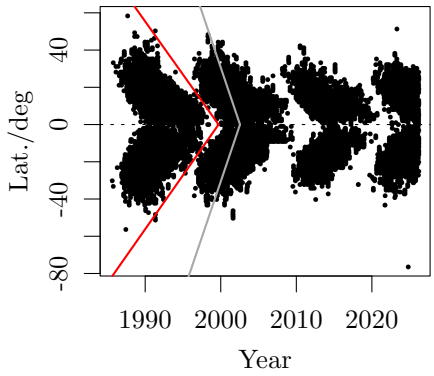


Fig. 1 Optimization of segmentation lines. Black dots represent the Sunspot group positions over time. The gray line indicates the initial condition at T_0, m_{01}, and m_{02} for the fit, whereas red lines depict the optimized result.

$|m_1|, |m_2| < 12\,\mathrm{deg/yrs}$ are bounded and assigned on the Northern and Southern hemispheres, respectively. The initial value of the temporal shift $T_{0g} \approx 1835 + 11g$ considers the group number g to move forward in the data set separating the individual solar cycles.

The distance $d_n = \sqrt{(L_n - x_s)^2 + (Y_n - y_s)^2}$ of an individual Sunspot group (L_n, Y_n) to the segmentation line is a simple orthogonal projection on that line. The corresponding intersection point (x_s, y_s) of the projection line $f(Y) : -m^{-1} \cdot (Y - Y_n) + L_n$ reads

$$x_s = \frac{m \cdot T_0 + L_n + m^{-1} Y_n}{m + m^{-1}} \tag{3}$$

The optimization then minimizes the penalty function $p_n \sim \mathrm{e}^{-d_n}(1 + m/5)$ as a measure of inverse distance, between points and corresponding segmentation lines and minimal slope. In fact the slope should be as small as possible whereby d_n is weighted exponentially. Figure 1 depicts the optimization of group separation of the last 30 yrs, where the gray line indicates the initial condition and red line the optimized result. The subdivision is straight forward but not perfect, indicated for example by several points around the year 1990 at $\pm 50°$ latitude which might be assigned differently when performing the suggested segmentation by [26, Fig. 2]. However, with a total sum of $\mathcal{O}(10^5)$ observed Sunspots, it is unlikely that such single distortions change the character of the spectrum. The final segmentation is depicted in Figure 2 where 18 individual cycles subdivided by a $>$ - shaped separation area are shown.

Implications for spectral decomposition

By structuring the data as $\{Y_i, L_i, P_i\}$ and because of the stochastic nature of Sunspot emergence, we create a non-evenly sampled 2D grid. Traditional Fourier Transforms are inapplicable due to the irregular sampling. Consequently, the 2D Lomb-Scargle Periodogram (LSM) is the necessary mathematical tool, as it allows for the extraction of periodic components directly from this arbitrary sampling of binary polarity events without the need for interpolation or any averaging technique.

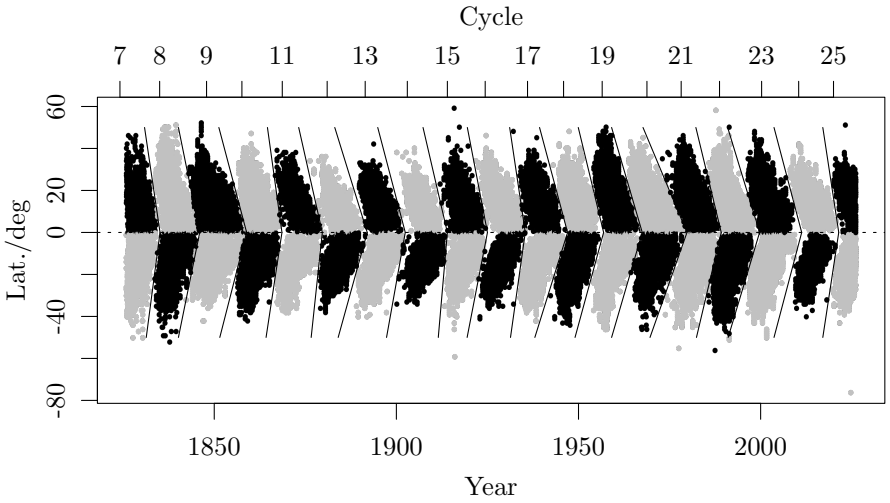


Fig. 2 Butterfly diagram of the Sunspot data. The separation of the individual wings took place according to the proposed procedure presented in [28]. The colored patches indicate the changing polarity of each cycle. The tilted segmentation lines depict the optimized borders between two cycles. Data is composed from [22, 27, 29] to cover ranges 1825–2016 up to present.

The range of the data set is given as a time span of $\Delta Y = 200\,\mathrm{yrs}$, a latitudinal coverage of $\Delta L = 135°$ and a total count of $N \approx 2.7 \cdot 10^5$. While the dimensions are restricted to latitude and time all duplicates were excluded with same latitude but different longitude. As a remark on data quality, historical observations might be affected by weather, night-side occlusion or observation technique [29], so that samples before 1825 are unsuited for the presented analysis.

Latitude is recorded with a resolution of 1°, which defines the maximum observable latitudinal frequency as $\max(f_{\mathrm{Lat}}) \leq \pm 0.5\,\mathrm{deg}^{-1}$. The frequency resolution then is limited by the observation window ΔL and reads $\Delta f_{\mathrm{Lat}} = \frac{1}{\Delta L} \approx 0.007\,\mathrm{deg}^{-1}$. The temporal frequency range is bounded by a maximum frequency of $\max(f_{\mathrm{Yrs}}) = 50\,\mathrm{yrs}^{-1}$, facilitated by the arbitrary sampling density of the underlying observations. Actually the temporal frequency increment can be estimated as $\Delta f_{\mathrm{Yrs}} = \Delta Y^{-1} = 0.005\,\mathrm{yrs}^{-1}$. Subsequently, a dynamical frequency stepping is introduced to oversample frequency space in a lower range of $f_{\mathrm{Yrs}}^{-1} \in [1\,\mathrm{yrs} \ldots 5000\,\mathrm{yrs}]$. Although, this lower bound is clearly out of a reasonable Fourier resolution, although it enables a better detection of lowest frequencies. Higher frequencies $f_{\mathrm{Yrs}} > 1\,\mathrm{yrs}^{-1}$ shall be sampled with Δf_{Yrs} respectively. Figure 3 summarizes the result of dynamic frequency stepping for both domains.

2.1 Butterfly Diagram

The Sunspot occurrence data as seen in Figure 2 depicts the dataset $\{Y_n, L_n, P_n\}$ and color coded the assigned field polarity value P_n (gray or black). In our analysis, we interpret each " wing" of this diagram as an individual wave packet propagating towards the equator. The segmentation procedure followed the suggestions from [28],

Table 1 Parameters of Segmentation Lines. The slopes $m_{1,2}$ are given in deg/year

T_0	m_1	m_2	T_0	m_1	m_2
1835.1	-11.8	13.2	1947.0	-6.5	5.6
1846.0	-8.5	8.5	1956.9	-7.2	6.4
1858.9	-6.6	6.8	1967.5	-5.9	5.9
1868.6	-12.6	11.4	1979.8	-4.1	4.9
1879.7	-7.7	16.3	1989.2	-7.2	7.3
1892.0	-5.6	6.3	1999.7	-5.7	5.8
1902.4	-6.6	9.7	2011.3	-6.6	6.6
1914.0	-7.5	20.0	2021.4	-11.4	11.4
1925.0	-9.1	9.0			
1935.4	-11.7	12.3			
Average		$\overline{m}_1 \approx -7.9\,\mathrm{deg/yr}$		$\overline{m}_2 \approx 9.3\,\mathrm{deg/yr}$	
Standard Dev.		$\sigma_1 = 2.44\,\mathrm{deg/yr}$		$\sigma_2 = 4.13\,\mathrm{deg/yr}$	

but with some simplifications leading only to minor miss-assignments for individual Sunspot groups as discussed in the previous section. In conjunction with traditional counting methods, we assign a binary polarity $P(Y_n, L_n) \to \{-1, 1\}$ to each Sunspot group. This assignment follows the Hale cycle logic [30], where the leading magnetic polarity of Sunspot groups reverses every approximately 11 years. Consequently, this assignment of different polarity lead to a period doubling. The full period of a 22 yrs Sunspot cycle is then called the Hale cycle.

The primary characteristic of the butterfly diagram is the equatorward migration of Sunspot emergence locations. Even very early mathematical models, see [4] as well as developed dynamo models, see [7, 9], indicate this migration as physical expression of a traveling wave. In a purely linear, unmodulated system, this migration would follow a constant slope (m). However, our segmentation procedure reveals that the slopes between individual cycles are not uniform. While we identify mean slopes of $\overline{m}_1 \approx -7.9\,\mathrm{deg/yr}$ (North) and $\overline{m}_2 \approx 8.94\,\mathrm{deg/yr}$ (South), there is significant cycle-to-cycle variation. Comparing $\overline{m}_1$ an $\overline{m}_2$ with a two sided t-test, we find, that both average slopes differ statistically significant with $p = \mathcal{O}(10^{-10})$. The interpretation is, that within the observed range both hemispheres are asymmetric to a certain amount. This is consistent with common literature, refer to [15] and with the spectral decomposition later on. The question is, how would this effect the spectral representation of the traveling wave. The average characteristic phase velocity of the northern and southern hemispherical wave might be estimated from the data by $\overline{v}_{1,2} \approx 1/\overline{m}_{1,2}$.

These fluctuating slopes, refer to standard deviations in Table 1, indicate that the phase velocity of the dynamo wave is not constant over secular timescales. This " wiggling" of the butterfly wings suggests a velocity modulation that must manifest as distinct spectral signatures—as side bands next to a carrier in the frequency domain.

Furthermore, the latitudinal range (the " amplitude" of the wing) varies significantly between cycles. Some solar cycles exhibit Sunspot emergence at latitudes exceeding 45°, while others remain confined to lower latitudes. This variation in the

latitudinal extent represents a spatial modulation of the wave's envelope. Combined with the temporal variations in cycle duration, these features lead us to the conclusion that the solar dynamo is a highly modulated traveling wave system. The "wiggles" in the butterfly wings and the breathing of the latitudinal range are not stochastic noise; they are the result of long-term periodicities ∼200 years which may be related to Gleissberg or Suess de Vries cycles acting upon the primary Hale-cycle carrier wave.

By viewing the butterfly diagram through this lens, we move away from seeing "cycles" as isolated pulses. Instead, we see a continuous, albeit modulated, wave. The spectral analysis that follows is specifically designed to decompose this modulation. The "wiggles" observed in the butterfly diagram are consistent with the off-diagonal peaks found in the two dimensional power spectrum.

3 Spectrum Analysis

By treating the Sunspot groups as a discrete sampling series of polarity events, we circumvent the need for temporal averaging and windowing, except the observation window. Nonetheless, this discrete and non-uniform sampling carries its own difficulties, as it can lead to aliasing and undesired higher harmonics. The multivariate Lomb-Scarge periodogram is recently discussed in [14]. It is specifically adapted to manage non-equidistant observations on a n–dimensional domain. As an advantage, the arbitrary sampling in combination with a two dimensional data set offers effectively suppressing false aliases and resolves true physical resonances of the system.

To ground the subsequent analysis, we briefly define the mathematical model behind the multivariate Lomb Scargle Method in two dimensions. For our dataset consisting of N binary observations $P_n \in \{-1, 1\}$ at arbitrary coordinates (Y_n, L_n) with $n = 1, \ldots, N$, we seek to determine the spectral power at any given kth frequency pair $(\omega_{\mathrm{Yrs},k}, \omega_{\mathrm{Lat},k})$. Here, $\omega_{\mathrm{Yrs},k} = 2\pi f_{\mathrm{Yrs},k}$ and $\omega_{\mathrm{Lat},k} = 2\pi f_{\mathrm{Lat},k}$ denote the temporal and spatial angular frequencies, respectively. The LSM is equivalent to finding the least-square-fit parameters of a linear wave model at each frequency pair. We model the expected polarity as:

$$P_n(Y_n, L_n) \sim \sum_k \left(A_k \cdot \cos\left(\phi_k(Y_n, L_n)\right) + B_k \cdot \sin\left(\phi_k(Y_n, L_n) + \epsilon_k\right)\right), \tag{4}$$

where P_n is given by the assigned patch polarity for the nth Sunspot group and A_k and B_k are the amplitudes of the wave components. The residual error is denoted with ϵ_k. The phase argument $\phi_k := \omega_{\mathrm{Yrs},k}\, Y_n + \omega_{\mathrm{Lat},k} L_n + \tau_k^*$ depends on time and longitude. Herein, the coefficient τ_k^* represents a shifting parameter, which makes sure that the trigonometric basis functions are orthogonal in the input data range, respectively to the observation window. k addresses one specific frequency pair of interest. To show the advantage and robustness of LSM the raw data is supplied without any further preprocessing, like windowing or tapering.

The selected frequencies $f_{\mathrm{Yrs},k}, f_{\mathrm{Lat},k}$ are given on a rectangular grid with dynamic distance so that large periods f^{-1} (small frequencies) are sampled more dense

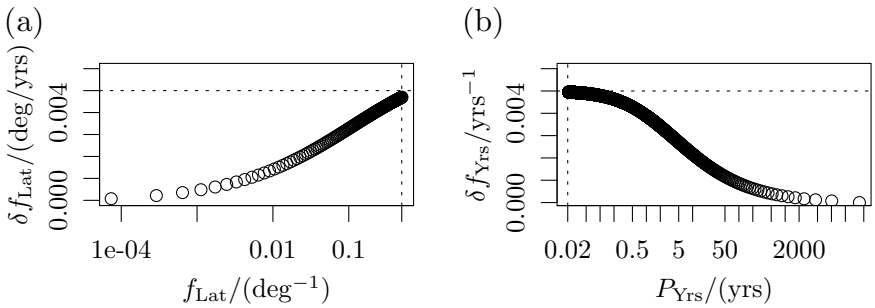


Fig. 3 Dynamic frequency grid. For dynamic oversampling of frequency space parameters a and k were adjusted according to (a) with $o = 1.75, a = 0.025$ and (b) with $o = 1, a = 0.01$ to maintain the stepping below Δf.

alongside the consecutive counter $k \in \mathbb{N}^+$ with $0 \leq k < K$. Subsequently, the frequency resolution can be sampled finer to better resolve the region in the range of $|f_{\mathrm{Lat}}| \approx 0$. With a certain extent the total number of analyzed frequencies is given by $K \geq o \cdot f_{\max}/\Delta f$. The factor o controls the oversampling and upper bound of the frequency space. To meet the dynamic resolution requirements the derivative function $\delta f : \mathrm{d}f(k)/\,\mathrm{d}k \sim \Delta f \cdot \left(1 + (k+1)^{-1}\right)^{-1}$ adjusts the distance between two frequencies according to $\delta f \in [0, \Delta f]$. Figure 3 displays the calculated frequencies, each for latitude and time. By integration the frequency vector can be calculated as

$$f(k) := \frac{K \cdot \Delta f}{a} \cdot \left((K-1) \cdot n - \log\left((K-1) \cdot k + 1\right)\right), \tag{5}$$

which is then tuned by model parameters accordingly. The lowest frequency for analysis depends on the parameter a and the oversampling parameter o.

The normalized power spectral density reads

$$\mathrm{psd_k} = \frac{N}{N-1} \frac{\left(A_k^2 + B_k^2\right)}{2\sigma_0^2} \tag{6}$$

where A_k and B_k denote the model coefficients for the kth frequency pair.

Each local maximum identified at the sampled frequency is optimized by a constrained "L-BFGS-B" method [31]. Finally, the most significant maxima are summarized in Table A1.

Two dimensional side band modulation

Central to this analysis is the identification of lines of constant phase velocity (v-lines) within the spectral domain. Consider the model equation Eq. 4, the evaluation of

$$\begin{aligned} \phi_k &= \omega_{\mathrm{Yrs},k}\, Y_n + \omega_{\mathrm{Lat},k} L_n \\ &= 0 \end{aligned}$$

for constant phase $\phi = 0$ directly leads to $v_k = -L/Y = \omega_{\mathrm{Yrs},k}/\omega_{\mathrm{Lat},k}$. Similar to one dimensional Fourier decomposition a complex structure can be represented as sum of individual components,

$$w(Y, L) = \sum_k C_k \cdot \mathrm{e}^{\mathrm{i}(\omega_{\mathrm{Yrs},k} Y + \omega_{\mathrm{Lat},k} L)}, \tag{7}$$

where C_k denotes the complex amplitude. In the spectral domain, a perfectly coherent traveling wave would produce power concentrated at a single pair (ω, k) and $(-\omega, -k)$. In two dimensions a plain wave is characterized by a point symmetric pair of peaks, with respect to the origin. However, if the wave is modulated in amplitude, phase, or propagation velocity, the spectral power is redistributed along a curve defined by the dispersion relation $\omega_{\mathrm{Lat}} = -v \cdot \omega_{\mathrm{Yrs}}$, which is a diagonal crossing the coordinate systems origin in the spectral domain. The key is, that phase velocity v keeps constant for all pairs $(\omega_{\mathrm{Yrs},k}, \omega_{\mathrm{Lat},k})$ along the same plain wave packet. In case of a variation in amplitude or position a modulated amplitude $C_k := f(Y, L)$ can handle the temporal or spatial dynamics of the pattern. Suppose a simple case with $C_k = C_0 \mathrm{e}^{\omega_1 Y}$ with $\omega_1 \ll \omega_{\mathrm{Yrs}}$ the resulting wave gains a carrier frequency at ω_{Lat} and a (single) side band modulation. In the result $w(Y, L) = C_0 \mathrm{e}^{\mathrm{i}((\omega_{\mathrm{Yrs},k} + \omega_1) Y + \omega_{\mathrm{Lat},k} L)}$ shows, that the specific frequency peak in the spectral plain deviates a bit from the average phase velocity. To identify the precise spots of amplitude maxima, oversampling of frequencies becomes necessary which is one of the main features of the Lomb Scargle Method, here in a multivariate flavor. In combination with the side band modulation, drift velocities serve as carrier and can be estimated as average v-line out of a spectrum, even if the corresponding wave pattern is modulated. The measurement procedure is patented by [32] and formally based on ideas like [33].

In the present two dimensional power spectrum of Sunspot data, a traveling wave does not appear as a solitary point, but as a distribution or ridge of power along a diagonal defined by: $v = (f_{\mathrm{Lat}} \cdot P_{\mathrm{Yrs}})^{-1} = \mathrm{const}$.These characteristic lines serve as " process fingerprints" , which are associated with the same underlying physical process, namely the equatorward migration of large-scale magnetic structures as predicted by dynamo-wave theory. In this sense, the observed distribution of peaks can be interpreted as the spectral signature of a modulated traveling wave, rather than a set of independent oscillations.

Due to the nature of the observations, the underlying signal is not band-limited in a strict signal-processing sense. The solar dynamo is sampled only through the discrete occurrence of sunspots, which represent a nonlinear and intermittent manifestation of the magnetic field at the surface. Consequently, no well-defined physical filtering mechanism exists that would impose a sharp spectral band limit. Instead, the spectrum reflects a superposition of contributions from multiple scales and modulation processes.

This has two important implications. First, spectral peaks that deviate from the primary phase-velocity relation or align along different slopes may indicate the presence of additional dynamical processes, such as latitudinal modulation, effect of differential rotation, or long-term variations in the morphology of the butterfly diagram. Second, the absence of strict band limitation leads to aliasing effects, whereby power associated with dominant structures is redistributed across the spectral domain.

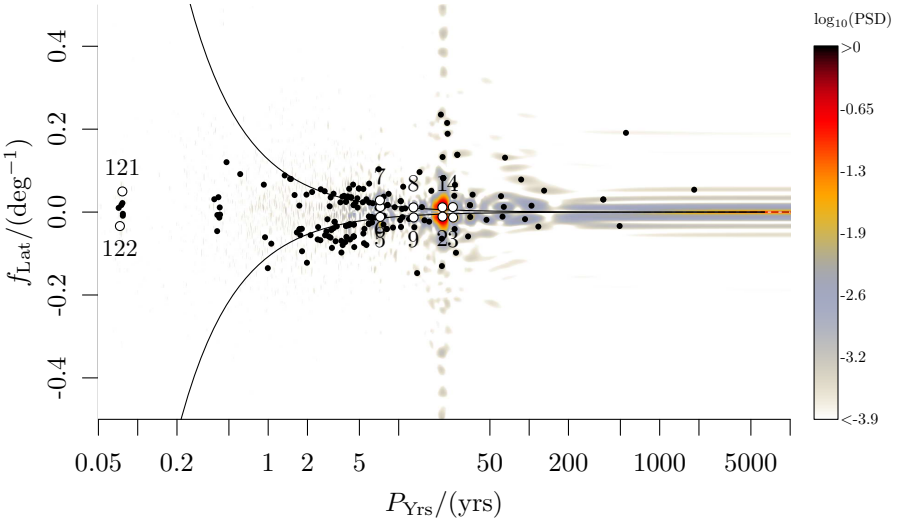


Fig. 4 2D LSM spectrum of the Sunspot data. The numbering of the individual maxima correspond to the ID in Table A1. The curved lines follow a path of constant phase velocity with $v = (f_{\mathrm{Lat}} P_{\mathrm{Yrs}})^{-1} = \text{const.}$ indicating a wave structure with a certain time dependence. The bold black lines depicts the mean waves with $v = (\overline{m}_{1,2})^{-1}$. The most dominant points (white dots) are located at $ID \in \{1 \ldots 4\}$. The Hale cycle splits into four components with a lower 21.6 yrs and an upper 26 yrs period pair.

In particular, periodicities related to solar rotation or the annual sampling imposed by the Earth's orbit ($P = 1\,\mathrm{yrs}$) may introduce secondary features or mirrored components.

In order to isolate the dominant wave pattern, we apply a selection criterion in frequency space, which is motivated by the maximum band limit related to sampling theory. Specifically, we restrict the analysis to latitudinal frequencies satisfying

$$|f_{\mathrm{Lat}}| > \frac{1}{2} \cdot \overline{v} \cdot f_{\mathrm{Yrs}}, \tag{8}$$

which suppresses contributions from large-scale, slowly varying latitudinal structures. The physically constrain yields, that only spectral components with statistical significance $\log_{10} p < -10$ are retained for frequencies above $|f_{\mathrm{Lat}}| > \overline{v} \cdot f_{\mathrm{Yrs}}$. This combined filtering emphasizes peaks associated with the dominant phase-velocity branch while reducing the influence of noise, aliasing and secondary processes.

We note that this selection does not impose a preferred phase velocity, but rather constrains the admissible region in frequency space based on the independently estimated drift velocity.

Main features of the diagram

Figure 4 shows the resulting two-dimensional spectral decomposition in a reciprocal logarithmic representation, which emphasizes periodicities across a wide range of timescales. Significant spectral peaks are indicated by numbered markers. All selected

Table 2 Common Peaks. Period values are given in years. Values above 100 yrs are affected by the low period resolution caused by the limited time span of Sunspot data. Therefore Hallstatt and Eddy cycle are very uncertain. The results from [34] refer to Schwabe cycle and therefore are doubled.

Process	Common Period	From spectrum	Ref.
Hallstatt	2000...2400	1838	2
Eddy	515	551	1
	350	369	1
Gleissberg	88 (80...150)	87, 93,104, 117	1,2
–	126, 128	130	3
Hale (Schwabe)	22.14 (11.07)	21.69 ± 2.4, 26 ± 3.4	2,8
	18...28		2
Sun Radius	10.8	10.7, 10.8	7
–	2×3.6	7.2	4
quasi-triennial osc.	2×3.9	7.7	4,5
Rieger	154 d	154 d, 155 d	6
Sun rotation	27 d	26 . . . 28 d	

(1) [35]; (2) [16]; (3) [36]; (4) [34, Fig. 6]; (5) [37]; (6) [13]; (7) [10]; (8) [2].

peaks satisfy a false-alarm probability (FAP) of $p < 10^{-10}$, ensuring that they are statistically distinguishable from noise.

The peak locations are obtained through a local optimization of the spectral amplitude, providing a refined estimate of their positions in frequency space. The numbering corresponds to the peak identifiers listed in Table A1, which summarizes approximately 200 prominent spectral components detected in the sunspot data.

It should be noted that the use of binary polarity encoding introduces higher harmonics into the spectrum. These harmonics may also appear with low false-alarm probabilities and must therefore be interpreted with care. In addition, periods exceeding about 100 yrs are affected by the limited temporal extent of the dataset, resulting in reduced spectral resolution and increased uncertainty. Consequently, long-term variations such as the Gleissberg or Suess–de Vries cycles can only be qualitatively assessed within the present analysis.

A projection of the spectrum onto the temporal axis yields good agreement with commonly reported solar periodicities. Table 2 summarizes the most prominent periods identified in this way and compares them with values reported in the literature.

The Hale Cycle

The most prominent signal, identified by the two main peaks for positive and negative latitude $ID \in \{1, 2, 3, 4\}$, represent the 22 yrs Hale cycle. Values from literature vary from 18 . . . 28 yrs ([16]), in case one dimensional solar activity data is investigated. The precise value of 22.14 yrs can be calculated by means of Fourier analysis of Sunspot number, refer to [2]. The presented spectral analysis provides actually two major periods, i. e. $P = \{21.69, 26\}$ yrs clearly separated by each other.

The typical Hale-Cycle then becomes the beat frequency of the two, as shown next. Taking the weighted average on the four peaks from the spectrum the Hale cycle yields

a period of

$$P_{\mathrm{Hale}} = \frac{\sum_{i=1}^{4} psd_i}{\sum_{i=1}^{4} psd_i \cdot f_{\mathrm{Yrs},i}} = (21.9 \pm 1.2)\,\mathrm{yrs}, \tag{9}$$

which is almost exactly (with some extent to frequency resolution) the period length we see in spectral analysis of Sunspot number, refer to [2, 34, 38]. This supports the argument, that the averaging, which is introduced with the Sunspot number R_z, smears these spectral peaks, so that they become one prominent averaged signal. Concerning the variation in amplitude the difference between the two frequencies lead to a periodic variation with $P_{\mathrm{diff}} \approx 128\,\mathrm{yrs}$. This number is recovered by [36] with a spectral analysis of ^{10}Be isotope measurements and falls into the range of Gleissberg process, and recovers the latitudinal modulation of sunspot occurrence (breathing) of the butterfly wings.

Moreover, this empirical finding integrates naturally with the conceptual framework of [39], who successfully demonstrated that long-term solar variations (such as the Suess-de Vries and Gleissberg cycles) can be modeled as mathematical beat periods between a stabilized Hale carrier and external planetary perturbations. It is demonstrated that a phase-stable 22.14 yrs Hale cycle can be physically locked by an 11.07 yrs periodic α-effect driven by planetary tidal forces. However, while this double-synchronization dynamo model treats the 22.14-year Hale cycle as an undivided, fundamental internal clock phase-locked by an 11.07-year planetary tide, our observation of a split Hale peak suggests an additional layer to the whole picture.

Besides dynamo theory, a speculative interpretation to the origin of the 11 yrs cycle is discussed by [38]. The author suggests that there is a connection between cosmological parameters like size of the Universe (Hubble Radius r_{H}) and Bohr radius of Hydrogen r_{B} respectively which influence the periods on a quantum scale. It is then shown, that the "theoretical Hale period" can be estimated as

$$P_{\mathrm{H}} \approx \frac{2}{\mathrm{c}_0} \cdot \left(r_{\mathrm{B}} \cdot r_{\mathrm{H}}^3\right)^{0.25} \approx 21.7\,\mathrm{yrs}, \tag{10}$$

which is exactly the most dominant period seen in the presented spectra, $P_{ID=1} = 21.69\,\mathrm{yrs}$, from Sunspot analysis.

Longer Periods

Next to that we can identify typical longer periods which are related to the Gleissberg-, Eddy process (see Table 2). The main advantage of a multivariate analysis, process separation, becomes present with the Hallstatt cycle, $ID = 191$ at $P_{\mathrm{Yrs}} = (1839 \pm 202)\,\mathrm{yrs}$. Here the separation from noise level at $f_{\mathrm{Lat}} = 0$ takes place, because the specific peak is inclined with a latitudinal frequency of about $f_{\mathrm{Lat}} \approx 5.4 \cdot 10^{-2}\,\mathrm{deg}^{-1}$. Of course the uncertainty of the period is rather bad on the time variation scale. In consequence, the meaning of that might be highly speculative with respect to the

limited observation range of 200 years. On the other side, the latitudinal resolution $\Delta L \approx 7{\cdot}10^{-3}\,\mathrm{deg}^{-1}$ is small enough to clearly distinguish the signal from $f_{\mathrm{Lat}} = 0$ noise sufficiently. Also the corresponding p value indicates a certain significance, because the peak separates well on the f_{Lat}–axis.

Shorter Periods

Short periods in the range of $P \approx 7.2\,\mathrm{yrs}$, may be harmonics of the Hale cycle. These are consistent with the findings of [34] and [40] and align partially with [12] (specifically $ID \in \{17, 22, 23, 53\}$ as doubled period). It should be noted that the base period P_{Hale} should be an integer multiple of its harmonics. This analysis supports that condition, as $21.6\,\mathrm{yrs} = 3.0 \cdot 7.2\,\mathrm{yrs}$.

Previous historical results often contradict this finding, as the typical Hale cycle of $22.14\,\mathrm{yrs}$ is not an integer multiple of the observed harmonics. However, as demonstrated above, P_{Hale} is a superposition of several distinct frequencies each accompanied by its own harmonics. These observed harmonics originate from both, grouped solar flares and Sunspot number time series. In particular, the peaks at $ID \in \{13, 41\}$ are corroborated by [37], who identified similar signals in 10.7 cm radio flux measurements, helioseismic frequency shifts, and Sunspot areas.

Even shorter periods are observed at $\approx 1.7\,\mathrm{yrs}$ ($ID = \{149, 188, 184\}$), pointing to the Quasi-Biennial Oscillation (QBO) discussed in [18, 40]. Within the limits of our spectral resolution, we identify these peaks in the range $P_{\mathrm{QBO}} = (1.723 \pm 0.06)\,\mathrm{yrs}$. This value further supports the harmonic hypothesis: the ratio $26\,\mathrm{yrs}/P_{\mathrm{QBO}} = 15.09$ suggests the 15th harmonic of the Hale cycle, which is consistent with an integer multiple of the second base period given the current frequency resolution. Since the QBO occurs primarily during Sunspot maxima, it may be regarded as a localized event. Consequently, its spectral signature is characterized by a low amplitude due to its sparse occurrence in the time series.

A recent work by [41] unified the short term and long term processes and explain solar activity by a self-consistent synchronization model of the solar dynamo. Hence such theoretical approaches investigate numerical insight into the solar processes, which can be found in solar activity data or historical geodata, the direct observation of Sunspot occurrence unifies all these periods into one spectral representation.

Day-scale oscillation

Figure 5 displays a Rieger-type oscillation associated with the peak group $ID \in 192, 193, 197$, consistent with previously reported periodicities (see [13, 18]).

In addition, the solar rotation period of approximately $P_{\mathrm{rot}} \approx 27\,\mathrm{d}$ manifests as a cluster of spectral peaks at $ID \in 121, 122$. In this region of the spectral plane, the maxima are not localized at a single latitudinal frequency but instead exhibit a spread along the ordinate. This behavior is consistent with solar differential rotation, which introduces a distribution of angular velocities and thus a continuum of effective drift velocities.

Notably, the peaks at $ID = 122$ (lower left) and $ID = 121$ (upper right) suggest the presence of a modulation with a characteristic center period $P_0 = 27.23\,\mathrm{d}$ which appears to be distinct from the primary Hale-cycle-related process. Additionally, the

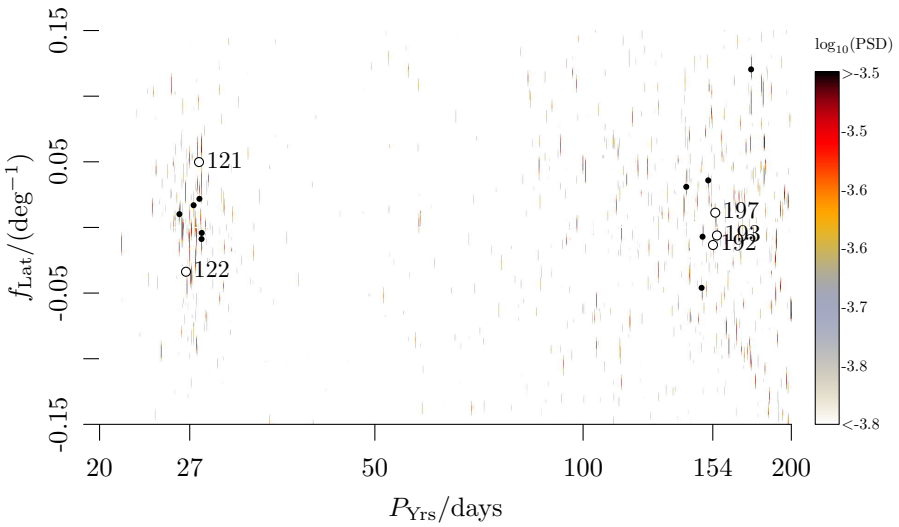


Fig. 5 Sunspot Spectrum of short term periods. This is a zoomed version of the spectrum in the rage of $20\,\mathrm{d} < P_{\mathrm{Yrs}} < 200\,\mathrm{d}$.

approximate point symmetry of these peaks supports their interpretation as modulated wave components.

Furthermore, solar rotation may act as a secondary modulation frequency. Within this framework, the observed nearby spectral peaks can be interpreted as alias or side band components arising from the interaction between rotational modulation and the underlying dynamo wave.

In summary, the two-dimensional spectral analysis not only recovers the well-established periodicities of solar activity, but also reveals their distinct organization in spectral space. While a subset of peaks aligns along characteristic phase-velocity ridges, suggesting the presence of a coherent propagating structure, other prominent signals—such as those associated with solar rotation and Rieger-type oscillations—remain clearly separated. This separation indicates that the solar activity spectrum consists of multiple dynamical components, only part of which may be attributed to a common underlying mechanism. The physical interpretation of the ridge-like structures, in particular, is addressed in the following section.

4 Traveling-Wave Interpretation of the Butterfly Diagram

The spectral analysis in Section 3 has shown that the dominant power in the two-dimensional spectrum is organized into structured distributions rather than isolated peaks. In particular, a subset of significant maxima aligns along characteristic phase-velocity relations, while other signals—such as those associated with solar rotation or Rieger-type oscillations—remain clearly separated in spectral space. This indicates that the observed variability of solar activity cannot be attributed to a single process,

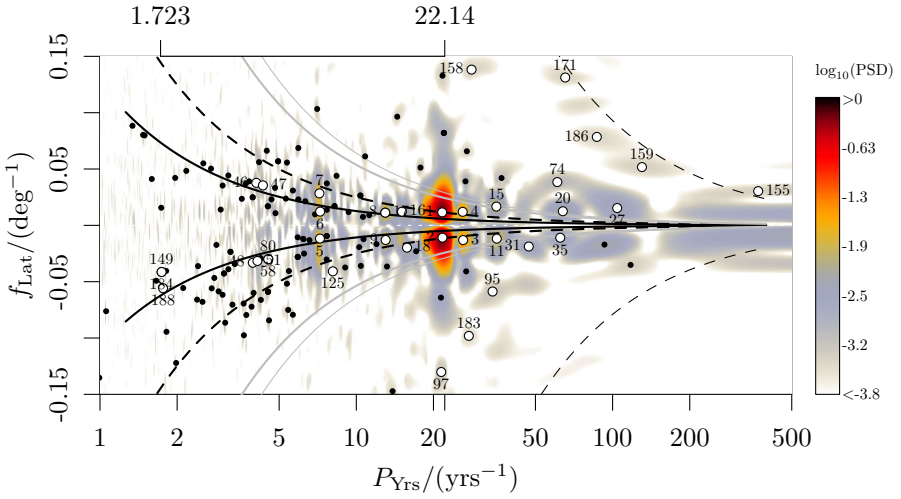


Fig. 6 Sunspot Spectrum with traveling waves. The lines indicate regions of constant phase velocity. Depending on the reference the drift velocities vary. The solid black corresponds to the average tilt of Sunspot patches in the butterfly diagram, thick black dashed refers to the unmodulated ideal Hale cycle, gray lines indicate results from drift measurements and thin dashed lines are speculative. The numbers correspond to the *ID* identifiers.

but instead reflects the superposition of distinct dynamical components, only part of which may be associated with a coherent propagating structure.

In the following, we focus on the ridge-like features identified in the spectrum and interpret them in terms of a modulated traveling wave underlying the Sunspot butterfly diagram. Within this framework, the 22-year Hale cycle is not represented by a single spectral line, but by an extended structure composed of a carrier component and its associated harmonics, all of which are organized along a common phase-velocity relation.

Since the solar cycle is inherently modulated and asymmetric [15], a broad spectrum characterized by numerous harmonics naturally emerges. The Sunspot distribution indicates that the complex, non-stationary structures of the individual wings in the butterfly diagram, e. g. exhibiting varying widths, heights, and orientations, are fundamentally tied to a dominant carrier period of P_{Hale} and its associated (sub-) harmonics. For periods with $P_{\mathrm{Lat}} > 22\,\mathrm{yrs}$, these long period features manifest mainly as a set of local maxima concentrated primarily along a horizontal line at $|f_{\mathrm{Lat}}| \approx 1.4 \cdot 10^{-2}\,\mathrm{deg}^{-1}$. Furthermore, the inclusion of the latitudinal dimension effectively spreads the spectral peaks vertically. This represents a significant advantage over traditional one-dimensional analyses, such as the Wolf or Sunspot number evaluations [42], where all signals project directly onto the $f_{\mathrm{Lat}} = 0$ axis. In consequence, all independent peaks of 1D spectral analysis, such as those identified by $ID \in \{1 \ldots 9, 15, 31, \ldots\}$, would collapse on the ordinate and become conflated.

Interpreting the butterfly diagram (Figure 2) as a superposition of modulated waves propagating toward the equator provides a natural framework for analyzing

the spectral structure. In this picture, the observed Sunspot distribution $P(Y, L)$ is modeled as a sum of wave-like components of the form Eq. 7 where the coefficients $C_k(Y, L)$ encode amplitude and phase modulation. The two-dimensional LSM then acts as a decomposition of this representation, resolving the contributing frequency pairs $(\omega_{\mathrm{Yrs},k}, \omega_{\mathrm{Lat},k})$ without requiring interpolation or averaging.

Within this framework, coherent propagation toward the equator corresponds to spectral power concentrated along lines of constant phase velocity, whereas temporal or spatial modulation gives rise to a redistribution of power into side band components.

A purely plain wave signal with a single dominant period, such as $P \approx 22\,\mathrm{yrs}$, would correspond to an isolated symmetric pair of peaks in spectral space. However, such a description is insufficient to capture the complex and evolving structure of the butterfly diagram. Conversely, a rigid pattern of Sunspot groups drifting uniformly toward the equator would manifest as a sequence of aligned peaks tracing a line of constant phase velocity, defined by $v = (f_{\mathrm{Lat}} P_{\mathrm{Yrs}})^{-1} = \mathrm{const}$. The observed spectrum exhibits neither of these limiting cases. Instead, it reveals a broadened ridge of enhanced power, indicating a coherent propagating structure whose phase velocity is approximately conserved, but subject to temporal and spatial modulation.

The finite width of this ridge reflects the non-stationary nature of the underlying process. Variations in cycle amplitude, duration, and latitudinal extent, which is clearly the case in Figure 2, introduce modulation of the traveling wave, which manifests in spectral space as side band structures distributed around a central phase-velocity line. In this interpretation, the ridge itself represents the carrier of the wave, while the surrounding peaks encode its modulation in both time and latitude. Consequently, the characteristic phase-velocity line (v-line) can be understood as the spectral signature of the average propagation of magnetic activity, whereas deviations from this line quantify the dynamical variability of the solar cycle.

Figure 4 illustrates several characteristic phase-velocity lines (v-lines) derived from the spectral maxima. The dominant Hale-cycle component, identified by peaks at $P_{\mathrm{Yrs}} = 21.634\,\mathrm{yrs}$ and $f_{\mathrm{Lat}} = 1.152 \cdot 10^{-2}\,\mathrm{deg}^{-1}$ ($ID \in \{1, 2\}$) , corresponds to a phase velocity of $v_{\mathrm{Hale}} = 4.012\,\mathrm{deg/yrs}$. This value represents an idealized single-frequency approximation, which is represented by the black dashed line in the graph. In contrast, the observed ridge spans a range of nearby phase velocities, reflecting the modulated nature of the underlying wave.

An independent estimate of the propagation velocity can be obtained from the slopes of the butterfly wings (Figure 2), yielding mean values $v_{1,2} \approx 1/\overline{m}_{1,2}$. The corresponding v-lines (solid black) align closely with regions of enhanced spectral power, providing direct evidence that the spectral ridge is linked to the observed equatorward drift of Sunspot activity.

The butterfly diagram clearly exhibits cycle-to-cycle variability in both slope and latitudinal extent, indicating that the phase velocity is not constant over time. This variability naturally leads to a distribution of spectral power around the average v-line, so that the spectral ridge appears. Within the modulation framework introduced above, the peaks located near this line, e.g. $P \approx 4$ or $ID \in \{46 \ldots 48, 51, 58, 80\}$, can be interpreted as side band components associated with the Hale-wave as carrier.

In contrast to a purely sinusoidal representation, this description accounts for the observed complexity of the Sunspot distribution, including the "wiggling" and amplitude variations of the butterfly wings.

The conclusion is that the Hale-cycle, with its main period at P_{Hale} might be described as a modulated set of coherent waves with minor prominent harmonics, specifically $ID \in \{5 \dots 7\}$ as 3rd harmonic and $ID \in \{88, 84\}$ as 15th harmonic. If so, peaks arranged around the characteristic v-line such as $ID \in \{3, 4, 5, 6, 7, 8, 9, 53, 83, 124, 162, 172, 188\}$, are directly coupled with the solar cycle. These individual side bands, see $ID \in \{5 \dots 7, 125\}$, are covered by the results of [34] investigating geomagnetic indices and Sunspot number time series.

While the ridge structure captures the modulated nature of the traveling wave, it is also instructive to compare with empirical drift laws derived from averaged Sunspot positions. For example, the relation $\lambda(t) = 28° e^{-12t/90}$ [43, Eq. (4)] implies a mean drift velocity of the (wing) centroid position with $v \approx 1.8622\,\text{deg/yrs}$. The corresponding v-line, bold gray in Figure 4, intersects several spectral maxima, indicating partial consistency with the observed propagation. The neighboring thin solid gray line is defined by $\overline{v} = 1.56\,\text{deg/yrs}$ as suggested by [44] investigating the same process of equatorial drift.

However, such averaged descriptions inherently smooth the underlying dynamics and therefore do not fully capture the coherent wave structure revealed by the two-dimensional spectral analysis.

As a speculation about other present waves, the thin dashed black line defined by the peaks $ID = \{155, 159, 171, 186\}$ might be related to a Gleissberg process. Surprisingly this curve follows $v_{\text{GB}} \sim \overline{m}_{1,2}$ law, which indicates a traveling wave perpendicular to the standard equatorial drift velocity. The corresponding line in the lower half plane of Figure 4 is not symmetric indicating the asymmetry between the hemispheres. And finally a remaining v-line could be defined by the points $ID = \{31, 35, 95, 97, 183\}$ and $ID = \{27, 74, 158\}$ which might belong to another (yet unidentified) process.

A key consequence of this interpretation is that spectral peaks corresponding to different temporal scales are not necessarily independent. Instead, peaks that lie along the same phase-velocity ridge can be understood as components of the same underlying traveling structure or same physical process.

This interpretation does not exclude the presence of additional dynamical processes, which may manifest as secondary ridges with different phase velocities. However, the existence of a dominant phase-velocity alignment strongly suggests that a large fraction of the observed variability is governed by a coherent propagating structure. Further investigations with respect to Rossby waves, are open if the longitude information of each Sunspot group is taken into account. Doing so, a three dimensional approach enables access to the meridional drift and a modal decomposition of such a wave pattern.

The existence of a coherent propagation velocity is consistent with the concept of dynamo waves in mean-field theory [4, 5]. In such models, the direction and speed of propagation are determined by the interplay between differential rotation and the α-effect.

While the present analysis does not directly infer the underlying dynamo parameters, the observed phase velocities and their hemispheric asymmetries provide empirical constraints that can be compared with theoretical predictions. In this sense, the spectral ridge identified here can be interpreted as an observational signature of the dynamo wave operating within the solar interior.

5 Conclusion

In this work, we introduced a two-dimensional spectral analysis of sunspot occurrence data spanning the period 1825–2025. By moving beyond traditional one-dimensional solar indices, which effectively act as a spatial low-pass filter, we preserve the full latitude–time structure of the butterfly diagram. The application of a multivariate Lomb–Scargle method to the irregularly sampled dataset with polarity encoding $P(Y, L) \in \{-1, 1\}$ enables a direct estimation of the two-dimensional power spectrum without interpolation or smoothing. The analysis is performed in the frequency domain $(f_{\mathrm{Yrs}}, f_{\mathrm{Lat}})$, where the coupling between temporal and spatial scales is retained.

The central result of our investigation is that solar activity spanning across a wide range of timescales can be interpreted as components of a single modulated traveling wave. The two-dimensional spectral decomposition reveals that enhanced power is preferentially concentrated along a region of approximately constant phase velocity, $v = (f_{\mathrm{Lat}} P_{\mathrm{Yrs}})^{-1}$,which represents the characteristic signature of a traveling wave. Importantly, this phase-velocity relation is not fitted to the spectral data, but independently derived from the observed equatorward drift of the butterfly diagram. The mean slopes of the segmented wings correspond to phase velocities that closely match the dominant spectral ridge. The agreement between both estimates provides strong evidence that the spectral ridge is directly linked to the physical propagation of magnetic activity.

Within this framework, periodicities commonly identified in solar activity can be interpreted as projections of an intrinsically two-dimensional structure onto the one-dimensional temporal axis. In contrast, the two-dimensional spectrum depicts the 22 yrs Hale cycle not as a single isolated peak, which is instead represented by a small cluster of nearby spectral components, for example at $P = \{21.7\,\mathrm{yrs}, 26\,\mathrm{yrs}\}$. When the latitudinal information is integrated out, as in traditional sunspot number analyses, these neighboring components contribute to a single dominant peak or beat frequency. In this sense, the commonly reported 22 yrs period corresponds to an effective or averaged representation of a more complex underlying structure.

This demonstrates that even the most prominent solar cycle is not strictly monochromatic, but exhibits a finite spectral width that reflects the dynamical variability of the underlying process.

Even longer periods of secular cycles like the Gleissberg cycle, show a clear tendency to align along several lines of constant phase velocity in the spectral domain. As these velocity lines serve as process fingerprints each, this seemingly disparate periods are physically coupled and may originate from a secondary process. To decide for an alternate wave signature or alias effect a further investigation with at least one additional domain, i. e. longitude information, is necessary.

A second key result is that the two-dimensional spectral representation enables a clear separation between propagating and non-propagating processes. While wave-like components associated with the butterfly diagram organize along phase-velocity ridges, other prominent signals, such as those related to solar rotation or Rieger-type oscillations, remain distinctly separated in spectral space. This distinction arises because stationary or purely temporal processes do not satisfy a phase-velocity relation, linking spatial and temporal frequencies. As a consequence, the two-dimensional approach provides a natural criterion to disentangle different physical mechanisms contributing to solar variability.

As a remark, the individual drift velocities for Sunspot migration from [43, 44] could not be recovered by an average phase velocity in the spectral decomposition and therefore do not describe a traveling wave in this context.

While the identification of long-term variability is limited by the finite temporal extent of the dataset, the observed phase-velocity alignment provides a robust framework for interpreting solar activity as a spatiotemporal process. Future work may extend this approach by incorporating longitudinal information, enabling a fully three-dimensional analysis. Such an extension would allow for the investigation of additional wave phenomena, including Rossby-type modes and meridional propagation, and may further clarify the origin of secondary spectral features.

Supplementary information. If your article has accompanying supplementary file/s please state so here.

Authors reporting data from electrophoretic gels and blots should supply the full unprocessed scans for key as part of their Supplementary information. This may be requested by the editorial team/s if it is missing.

Please refer to Journal-level guidance for any specific requirements.

Acknowledgements. The author like to thank Rainer Arlt from Astrophysical Institute Potsdam providing the Sunspot data and Frank Stefani, Andre Gieseke from HZDR as well as Albrecht Löhr from DHSN for many fruitful discussions.

Declarations

Declarations

Funding Not applicable
Conflict of interest/Competing interests The author declares that there are no conflicts of interest or competing interests.
Ethics approval and consent to participate Not applicable
Consent for publication The author consents to the publication of this manuscript in *Solar Physics*.
Data availability The consolidated sunspot data used in this study are compiled from the Royal Greenwich Observatory–USAF/NOAA (SOON) archives, historical observations by Schwabe and Spörer, as referenced in the text, and recent NOAA records. All data are publicly accessible via the URLs provided in the footnotes.
Materials availability Not applicable

Code availability Not applicable
Author contribution MS performed the data preparation, implemented the multivariate Lomb–Scargle periodogram, conducted the spectral analysis, and wrote the manuscript.

Editorial Policies for:

Springer journals and proceedings: https://www.springer.com/gp/editorial-policies

Nature Portfolio journals: https://www.nature.com/nature-research/editorial-policies

Scientific Reports: https://www.nature.com/srep/journal-policies/editorial-policies

BMC journals: https://www.biomedcentral.com/getpublished/editorial-policies

Appendix A Extendet Data

Table A1: Significant peaks of the Sunspot spectrum

ID	P_{Yrs}/yrs	$\pm\Delta P$/yrs	$\frac{f_{\mathrm{Lat}}}{10^{-2}\cdot\mathrm{deg}}$	$PSD \cdot 10^3$	$\log_{10}(p)$
1	21.631	1.172	1.152	604.132	< -50
2	21.690	1.179	-1.090	595.073	< -50
3	26.115	1.711	-1.308	47.387	< -50
4	26.017	1.698	1.200	38.112	< -50
5	7.212	0.130	-1.172	27.076	< -50
6	7.226	0.130	1.222	25.483	< -50
7	7.181	0.129	2.836	20.715	< -50
8	12.972	0.421	1.124	19.960	< -50
9	13.017	0.424	-1.299	18.158	< -50
10	13.017	0.424	-1.299	18.158	< -50
11	35.337	3.144	-1.179	11.838	< -50
12	6.897	0.119	0.984	10.306	< -50
13	7.673	0.147	-0.945	11.998	< -50
14	7.674	0.147	1.379	11.002	< -50
15	35.186	3.117	1.667	9.558	< -50
16	15.066	0.568	1.210	7.093	< -50
17	12.972	0.421	1.124	19.960	< -50
18	15.769	0.622	-1.980	6.136	< -50
19	7.654	0.146	-3.030	6.626	< -50
20	63.946	10.483	1.252	5.844	< -50

ID	P_{Yrs}/yrs	$\pm\Delta P$/yrs	$\frac{f_{\mathrm{Lat}}}{10^{-2}\cdot\mathrm{deg}}$	$PSD \cdot 10^3$	$\log_{10}(p)$
21	6.216	0.097	-1.209	4.766	< -50
22	92.938	22.807	-1.709	4.772	< -50
23	7.673	0.147	-0.945	11.998	< -50
24	6.216	0.097	-1.209	4.766	< -50
25	7.212	0.130	-1.172	27.076	< -50
26	5.941	0.088	2.306	4.086	< -50
27	104.202	29.096	1.534	3.905	< -50
28	8.223	0.169	1.706	3.922	< -50
29	17.122	0.734	-2.302	3.996	< -50
30	7.212	0.130	-1.172	27.076	< -50
31	47.089	5.617	-1.876	3.311	< -50
32	26.836	1.807	-4.085	3.237	< -50
33	6.253	0.098	-2.507	3.529	< -50
34	6.567	0.108	-1.316	4.519	< -50
35	62.472	9.993	-1.099	3.181	< -50
36	21.631	1.172	1.152	604.132	< -50
37	6.325	0.100	2.137	2.933	< -50
38	7.181	0.129	2.836	20.715	< -50
39	5.906	0.087	-1.061	2.956	< -50
40	21.393	1.146	-6.417	2.794	< -50
41	7.673	0.147	3.720	3.146	< -50
42	5.910	0.087	-2.798	2.352	< -50
43	11.993	0.360	-1.664	2.589	< -50
44	10.672	0.285	-1.224	2.177	< -50
45	10.616	0.282	0.752	2.195	< -50
46	4.072	0.041	3.772	2.066	< -50
47	4.322	0.047	3.547	2.013	< -50
48	3.947	0.039	-3.317	1.874	< -50
49	10.268	0.264	-1.932	1.767	< -50
50	9.331	0.218	1.183	2.187	< -50
51	4.113	0.042	-3.160	1.783	< -50
52	13.177	0.434	-3.656	1.803	< -50
53	4.234	0.045	-2.926	1.678	< -50
54	4.516	0.051	1.693	1.807	< -50
55	4.670	0.054	2.305	1.511	< -50
56	12.972	0.421	1.124	19.960	< -50
57	10.416	0.271	-3.597	1.602	< -50
58	4.533	0.051	-3.001	1.539	< -50
59	21.964	1.209	8.203	1.449	< -50
60	7.212	0.130	-1.172	27.076	< -50

ID	P_{Yrs}/yrs	$\pm\Delta P$/yrs	$\frac{f_{\mathrm{Lat}}}{10^{-2}\cdot\mathrm{deg}}$	$PSD\cdot 10^3$	$\log_{10}(p)$
61	21.964	1.209	8.203	1.449	$<$ -50
62	4.234	0.045	-2.926	1.678	$<$ -50
63	7.226	0.130	1.222	25.483	$<$ -50
64	35.186	3.117	1.667	9.558	$<$ -50
65	10.373	0.269	2.645	1.560	$<$ -50
66	11.233	0.315	0.901	1.351	$<$ -50
67	26.664	1.784	3.906	1.341	$<$ -50
68	21.964	1.209	8.203	1.449	$<$ -50
69	4.174	0.044	5.611	1.299	$<$ -50
70	4.113	0.042	-3.160	1.783	$<$ -50
71	4.516	0.051	1.693	1.807	$<$ -50
72	4.839	0.058	1.079	1.666	$<$ -50
73	7.181	0.129	2.836	20.715	$<$ -50
74	60.871	9.475	3.840	1.089	$<$ -50
75	3.046	0.023	-4.271	1.070	$<$ -50
76	1.056	0.003	-7.618	1.049	-50
77	9.049	0.205	-3.741	0.967	-49
78	8.223	0.169	1.706	3.922	-48
79	3.168	0.025	4.427	0.958	-47
80	4.533	0.051	-3.001	1.539	-47
81	5.659	0.080	3.089	0.931	-47
82	3.943	0.039	2.489	0.868	-44
83	3.357	0.028	-3.437	0.847	-42
84	3.080	0.024	-8.642	0.850	-42
85	5.910	0.087	-2.798	2.352	-41
86	4.243	0.045	-6.616	0.858	-41
87	3.046	0.023	-4.271	1.070	-40
88	3.975	0.039	-5.993	0.836	-39
89	493.169	1173.423	-3.362	0.784	-39
90	5.940	0.088	6.867	0.777	-38
91	36.867	3.424	4.200	0.802	-37
92	4.522	0.051	-5.895	0.815	-37
93	4.522	0.051	-5.895	0.815	-36
94	3.010	0.023	3.532	0.764	-36
95	34.022	2.913	-5.872	0.732	-35
96	21.058	1.111	23.517	0.718	-34
97	21.450	1.153	-13.017	0.750	-34
98	7.212	0.130	-1.172	27.076	-33
99	4.565	0.052	-8.432	0.706	-32
100	3.228	0.026	-2.347	0.667	-32

ID	P_{Yrs}/yrs	$\pm\Delta P$/yrs	$\frac{f_{\mathrm{Lat}}}{10^{-2}\cdot\mathrm{deg}}$	$PSD \cdot 10^3$	$\log_{10}(p)$
101	21.690	1.179	-1.090	595.073	-32
102	17.799	0.793	5.128	0.671	-31
103	5.459	0.074	-4.057	0.710	-31
104	3.575	0.032	2.356	0.660	-31
105	2.512	0.016	-6.787	0.649	-31
106	2.413	0.015	-3.618	0.646	-31
107	10.373	0.269	2.645	1.560	-30
108	4.322	0.047	3.547	2.013	-30
109	2.171	0.012	4.836	0.633	-30
110	4.522	0.051	-5.895	0.815	-30
111	3.703	0.034	3.713	0.709	-30
112	7.212	0.130	-1.172	27.076	-29
113	5.910	0.087	-2.798	2.352	-29
114	4.473	0.050	6.625	0.709	-28
115	3.722	0.035	-7.955	0.614	-27
116	5.362	0.072	-5.180	0.606	-27
117	4.819	0.058	3.327	0.661	-27
118	23.510	1.386	21.498	0.593	-27
119	3.287	0.027	-7.039	0.583	-27
120	2.903	0.021	-5.859	0.595	-27
121	0.076	0.000	4.980	0.640	-27
122	0.073	0.000	-3.377	0.662	-26
123	7.212	0.130	-1.172	27.076	-26
124	2.712	0.018	5.033	0.568	-25
125	8.099	0.164	-4.081	0.638	-25
126	3.634	0.033	-6.941	0.634	-25
127	5.364	0.072	5.573	0.548	-24
128	1.965	0.010	4.211	0.566	-24
129	1.493	0.006	7.988	0.545	-24
130	5.423	0.073	-7.508	0.541	-24
131	0.076	0.000	2.179	0.527	-23
132	8.099	0.164	-4.081	0.638	-23
133	3.818	0.036	3.906	0.530	-23
134	3.007	0.023	-6.163	0.569	-23
135	0.077	0.000	-0.419	0.652	-23
136	3.228	0.026	-2.347	0.667	-23
137	4.953	0.061	5.687	0.543	-23
138	0.073	0.000	-3.377	0.662	-22
139	21.695	1.179	13.282	0.519	-22
140	2.530	0.016	5.500	0.528	-22

ID	P_{Yrs}/yrs	$\pm\Delta P$/yrs	$\frac{f_{\mathrm{Lat}}}{10^{-2}\cdot\mathrm{deg}}$	$PSD\cdot 10^3$	$\log_{10}(p)$
141	7.035	0.124	10.329	0.558	-22
142	117.570	37.790	-3.512	0.506	-21
143	0.077	0.000	-0.884	0.493	-21
144	5.658	0.080	-7.934	0.498	-21
145	0.479	0.001	12.040	0.512	-21
146	4.953	0.061	5.687	0.543	-21
147	23.712	1.409	18.889	0.485	-21
148	0.071	0.000	1.013	0.508	-21
149	1.739	0.008	-4.140	0.514	-21
150	21.690	1.179	-1.090	595.073	-21
151	0.075	0.000	1.691	0.490	-21
152	8.373	0.175	4.397	0.486	-21
153	2.846	0.020	-1.735	0.565	-20
154	3.170	0.025	-3.894	0.482	-20
155	369.876	2336.780	3.037	0.484	-20
156	1.812	0.008	-4.044	0.517	-20
157	28.158	1.991	13.823	0.498	-20
158	28.158	1.991	13.823	0.498	-20
159	130.174	47.336	5.172	0.483	-20
160	3.903	0.038	-7.223	0.478	-20
161	3.947	0.039	-3.317	1.874	-20
162	1.339	0.004	8.837	0.467	-20
163	14.450	0.522	9.644	0.474	-20
164	2.112	0.011	-5.564	0.481	-19
165	369.872	2336.435	3.037	0.484	-19
166	5.312	0.071	2.373	0.551	-19
167	0.926	0.002	6.613	0.456	-19
168	3.943	0.039	2.489	0.868	-19
169	0.610	0.001	9.161	0.489	-18
170	1.733	0.008	1.563	0.447	-18
171	65.323	10.951	13.122	0.452	-18
172	1.473	0.005	8.023	0.451	-18
173	1.658	0.007	-4.920	0.451	-18
174	10.825	0.293	6.121	0.450	-18
175	3.642	0.033	-9.757	0.437	-17
176	2.728	0.019	-5.593	0.440	-17
177	1.817	0.008	-9.447	0.431	-17
178	13.852	0.480	-14.719	0.423	-17
179	26.996	1.829	6.575	0.440	-17
180	2.958	0.022	1.398	0.696	-17

ID	$P_{\mathrm{Yrs}}/\mathrm{yrs}$	$\pm\Delta P/\mathrm{yrs}$	$\frac{f_{\mathrm{Lat}}}{10^{-2}\cdot\mathrm{deg}}$	$PSD\cdot 10^3$	$\log_{10}(p)$
181	1.981	0.010	-12.214	0.412	-17
182	2.392	0.014	-6.591	0.415	-16
183	27.486	1.896	-9.811	0.412	-16
184	1.739	0.008	-4.140	0.514	-16
185	0.993	0.002	-13.526	0.441	-16
186	86.795	19.747	7.846	0.409	-16
187	2.793	0.019	-4.669	0.495	-16
188	1.762	0.008	-5.576	0.416	-16
189	0.946	0.002	-6.073	0.425	-16
190	1.593	0.006	4.113	0.416	-16
191	0.415	0.000	3.585	0.399	-13
192	0.422	0.000	-1.336	0.356	-13
193	0.428	0.000	-0.610	0.354	-13
194	0.406	0.000	-4.600	0.343	-13
195	0.408	0.000	-0.707	0.350	-13
196	0.386	0.000	3.095	0.370	-11
197	0.425	0.000	1.122	0.305	-10
198	1838.662	420.224	5.396	0.297	-10
199	551.899	844.694	19.117	0.171	-2

References

[1] Schwabe, H., Schwabe, H.: Sonnen — Beobachtungen im Jahre 1843. Astronomische Nachrichten **21**(15), 234–235 (1844) https://doi.org/10.1002/asna.18440211505

[2] Dicke, R.H.: Is there a chronometer hidden deep in the Sun? Nature **276**(5689), 676–680 (1978) https://doi.org/10.1038/276676b0

[3] Hale, G.E.: On the Probable Existence of a Magnetic Field in Sun-Spots. The Astrophysical Journal **28**, 315 (1908) https://doi.org/10.1086/141602

[4] Parker, E.N.: THE SOLAR HYDROMAGNETIC DYNAMO. Proceedings of the National Academy of Sciences of the United States of America **43**(1), 8–14 (1957)

[5] Yoshimura, H.: Solar-cycle dynamo wave propagation. The Astrophysical Journal **201**, 740–748 (1975) https://doi.org/10.1086/153940

[6] Popova, E.P., Sokoloff, D.D.: The solar cycle from data on the large-scale surface magnetic field and solar-dynamo theory. Astronomy Reports **54**(11), 1042–1046 (2010) https://doi.org/10.1134/S1063772910110090

[7] Kitchatinov, L.L.: Do dynamo-waves propagate along isorotation surfaces?

Astronomy & Astrophysics **394**(3), 1135–1139 (2002) https://doi.org/10.1051/0004-6361:20021156

[8] Hathaway, D.H., Nandy, D., Wilson, R.M., Reichmann, E.J.: Evidence That a Deep Meridional Flow Sets the Sunspot Cycle Period. The Astrophysical Journal **589**(1), 665 (2003) https://doi.org/10.1086/374393

[9] Schüssler, M., Schmitt, D.: Does the butterfly diagram indicate a solar flux-transport dynamo? Astronomy & Astrophysics **421**(1), 349–351 (2004) https://doi.org/10.1051/0004-6361:20041302-1

[10] Qu, Z.-N., Feng, W., Liang, H.-F.: Periodicity of the solar radius revisited by using empirical mode decomposition and the Lomb–Scargle method. Research in Astronomy and Astrophysics **15**(6), 879–888 (2015) https://doi.org/10.1088/1674-4527/15/6/010

[11] Laclare, F., Delmas, C., Coin, J.P., Irbah, A.: Measurements and variations of the solar diameter. Solar Physics **166**(2), 211–229 (1996) https://doi.org/10.1007/BF00149396

[12] Deng, H., Mei, Y., Wang, F.: Periodic variation and phase analysis of grouped solar flare with sunspot activity. Research in Astronomy and Astrophysics **20**(2), 022 (2020) https://doi.org/10.1088/1674-4527/20/2/22

[13] Rieger, E., Share, G.H., Forrest, D.J., Kanbach, G., Reppin, C., Chupp, E.L.: A 154-day periodicity in the occurrence of hard solar flares? Nature **312**(5995), 623–625 (1984) https://doi.org/10.1038/312623a0

[14] Seilmayer, M., Wondrak, T., Garcia, F.: Multivariate Frequency and Amplitude Estimation for Unevenly Sampled Data Using and Extending the Lomb–Scargle Method. Sensors **25**(21), 6535 (2025) https://doi.org/10.3390/s25216535

[15] Hathaway, D.H.: The Solar Cycle. Living Reviews in Solar Physics **12**(1), 4 (2015) https://doi.org/10.1007/lrsp-2015-4

[16] Usoskin, I.G.: A history of solar activity over millennia. Living Reviews in Solar Physics **14**(1), 3 (2017) https://doi.org/10.1007/s41116-017-0006-9

[17] Kolotkov, D.Y., Anfinogentov, S.A., Nakariakov, V.M.: Empirical mode decomposition analysis of random processes in the solar atmosphere. Astronomy & Astrophysics **592**, 153 (2016) https://doi.org/10.1051/0004-6361/201628306

[18] Velasco Herrera, V.M., Pérez-Peraza, J., Soon, W., Márquez-Adame, J.C.: The quasi-biennial oscillation of 1.7 years in ground level enhancement events. New Astronomy **60**, 7–13 (2018) https://doi.org/10.1016/j.newast.2017.09.007

[19] Clette, F., Svalgaard, L., Vaquero, J.M., Cliver, E.W.: Revisiting the Sunspot

Number. A 400-Year Perspective on the Solar Cycle. Space Science Reviews **186**, 35–103 (2014) https://doi.org/10.1007/s11214-014-0074-2

[20] Willis, D.M., Coffey, H.E., Henwood, R., Erwin, E.H., Hoyt, D.V., Wild, M.N., Denig, W.F.: The Greenwich Photo-heliographic Results (1874 – 1976): Summary of the Observations, Applications, Datasets, Definitions and Errors. Solar Physics **288**(1), 117–139 (2013) https://doi.org/10.1007/s11207-013-0311-y

[21] Willis, D.M., Wild, M.N., Warburton, J.S.: Re-examination of the Daily Number of Sunspot Groups for the Royal Observatory, Greenwich (1874 – 1885). Solar Physics **291**(9), 2519–2552 (2016) https://doi.org/10.1007/s11207-016-0856-7

[22] Arlt, R., Leussu, R., Giese, N., Mursula, K., Usoskin, I.G.: Sunspot positions and sizes for 1825-1867 from the observations by Samuel Heinrich Schwabe. Monthly Notices of the Royal Astronomical Society **433**, 3165–3172 (2013) https://doi.org/10.1093/mnras/stt961

[23] Spoerer, G.: Mémoires et observations. Sur les différences que présentent l'hémisphère nord et l'hémisphère sud du soleil. Bulletin Astronomique, Serie I **6**, 60–63 (1889)

[24] Spoerer, F.W.G., Maunder, E.W.: Prof. Spoerer's researches on Sun-spots. Monthly Notices of the Royal Astronomical Society **50**, 251 (1890) https://doi.org/10.1093/mnras/50.4.251

[25] Diercke, A., Arlt, R., Denker, C.: Digitization of sunspot drawings by Spörer made in 1861-1894: Digitization of sunspot drawings by Spörer made in 1861-1894. Astronomische Nachrichten **336**(1), 53–62 (2015) https://doi.org/10.1002/asna.201412138

[26] Leussu, R., Usoskin, I.G., Pavai, V.S., Diercke, A., Arlt, R., Denker, C., Mursula, K.: Wings of the butterfly: Sunspot groups for 1826–2015. Astronomy & Astrophysics **599**, 131 (2017) https://doi.org/10.1051/0004-6361/201629533

[27] Solar Region Summary | NOAA / NWS Space Weather Prediction Center. https://www.swpc.noaa.gov/products/solar-region-summary#

[28] Leussu, R., Usoskin, I.G., Arlt, R., Mursula, K.: Properties of sunspot cycles and hemispheric wings since the 19th century. Astronomy & Astrophysics **592**, 160 (2016) https://doi.org/10.1051/0004-6361/201628335

[29] Arlt, R., Vaquero, J.M.: Historical sunspot records. Living Reviews in Solar Physics **17**(1), 1 (2020) https://doi.org/10.1007/s41116-020-0023-y

[30] Hale, G.E., Ellerman, F., Nicholson, S.B., Joy, A.H.: The Magnetic Polarity of Sun-Spots. The Astrophysical Journal **49**, 153 (1919) https://doi.org/10.1086/142452

[31] Zhu, C., Byrd, R.H., Lu, P., Nocedal, J.: L-BFGS-B: FORTRAN Subroutines for Large-Scale Bound Constrained Optimization. Technical report, Northwerstern University, Evanston, USA (1994)

[32] Seilmayer, M., Anders, S.: VERFAHREN UND VORRICHTUNG ZUM BESTIMMEN VON VERSCHIEBUNGSPARAMETERN SOWIE VORRICHTUNG ZUR STRÖMUNGSANALYSE. DE102021117407B42023.01.26, January 2023

[33] Willert, C.E., Gharib, M.: Digital particle image velocimetry. Experiments in Fluids **10**(4), 181–193 (1991) https://doi.org/10.1007/BF00190388

[34] Prestes, A., Rigozo, N.R., Echer, E., Vieira, L.E.A.: Spectral analysis of sunspot number and geomagnetic indices (1868–2001). Journal of Atmospheric and Solar-Terrestrial Physics **68**(2), 182–190 (2006) https://doi.org/10.1016/j.jastp.2005.10.010

[35] McCracken, K., Beer, J., Steinhilber, F., Abreu, J.: The Heliosphere in Time. Space Science Reviews **176**(1-4), 59–71 (2013) https://doi.org/10.1007/s11214-011-9851-3

[36] Ogurtsov, M.G., Nagovitsyn, Y.A., Kocharov, G.E., Jungner, H.: LONG-PERIOD CYCLES OF THE SUN'S ACTIVITY RECORDED IN DIRECT SOLAR DATA AND PROXIES, 24 (2002)

[37] Kolotkov, D.Y., Broomhall, A.-M., Nakariakov, V.M.: Hilbert–Huang transform analysis of periodicities in the last two solar activity cycles. Monthly Notices of the Royal Astronomical Society **451**(4), 4360–4367 (2015) https://doi.org/10.1093/mnras/stv1253

[38] Kotov, V.A., Sanchez, F.M., Bizouard, K.: On possible cosmic origin of the 11-year solar cycle. Bulletin of the Crimean Astrophysical Observatory **108**(1), 36–45 (2012) https://doi.org/10.3103/S0190271712010123

[39] Stefani, F., Horstmann, G.M., Mamatsashvili, G., Weier, T., Abastumani Astrophysical Observatory, Abastumani 0301, Georgia: Cosmic magnetic fields in theory and experiment: The role of harmonic forcings **61**(1), 33–42 https://doi.org/10.22364/mhd.61.1-2.4

[40] Kane, R.P.: Quasi-biennial and quasi-triennial oscillations in geomagnetic activity indices. Annales Geophysicae **15**(12), 1581–1594 (1997) https://doi.org/10.1007/s00585-997-1581-1

[41] Stefani, F., Horstmann, G.M., Mamatsashvili, G., Weier, T.: Adding Further Pieces to the Synchronization Puzzle: QBO, Bimodality, and Phase Jumps. Solar Physics **300**(8), 110 (2025) https://doi.org/10.1007/s11207-025-02521-0

[42] Scargle, J.D., Wagner, S.M.: Studies in Astronomical Time Series Analysis. VIII. The Double Lomb–Scargle Periodogram and Super Resolution. The Astrophysical Journal **999**(1), 84 (2026) https://doi.org/10.3847/1538-4357/ae40b9

[43] Hathaway, D.H.: A Standard Law for the Equatorward Drift of the Sunspot Zones. Solar Physics **273**(1), 221–230 (2011) https://doi.org/10.1007/s11207-011-9837-z

[44] Li, K.J., Yun, H.S., Gu, X.M.: Latitude Migration of Sunspot Groups. The Astronomical Journal **122**(4), 2115 (2001) https://doi.org/10.1086/323089

Supplementary Files

This is a list of supplementary files associated with this preprint. Click to download.

- SupMat.zip